nature synthesis

Article

https://doi.org/10.1038/s44160-023-00442-z

Surface-confined two-dimensional mass transport and crystal growth on monolayer materials

Received: 7 March 2023

Accepted: 16 October 2023

Published online: 27 November 2023



Check for updates

Yanyu Jia ^{1,7} M, Fang Yuan ^{2,7}, Guangming Cheng ³, Yue Tang¹, Guo Yu ^{1,4}, Tiancheng Song © 1, Pengjie Wang © 1, Ratnadwip Singha © 2, Ayelet J. Uzan-Narovlansky¹, Michael Onyszczak ¹, Kenji Watanabe ⁵, Takashi Taniguchi⁶, Nan Yao³, Leslie M. Schoop **©**² ≥ & Sanfeng Wu **©**¹ ≥

Conventional vapour deposition or epitaxial growth of two-dimensional (2D) materials and heterostructures is conducted in a large chamber in which masses transport from the source to the substrate. Here we report a chamber-free, on-chip approach for growing 2D crystalline structures directly in a nanoscale surface-confined 2D space. The method is based on the surprising discovery of the rapid, long-distance, non-Fickian transport of a uniform layer of atomically thin palladium on a monolayer crystal of tungsten ditelluride at temperatures well below the known melting points of all the materials involved. The nanoconfined growth realizes the controlled formation of a stable 2D crystalline material, Pd₇WTe₂, when the monolayer seed is either free-standing or fully encapsulated in a van der Waals stack. The approach is generalizable and compatible with nanodevice fabrication, promising to greatly expand the library of 2D materials and their functionalities.

The development of two-dimensional (2D) quantum materials and structures¹⁻⁸ is providing strong new impetus to a variety of fields in physics, engineering and chemistry. A computational survey of known layered bulk compounds has indicated that there are more than 1,000 layered van der Waals (vdW) crystals that can potentially be created down to the monolayer limit. Indeed, extensive efforts have been devoted to creating and optimizing 2D crystals in this library, especially graphene, boron nitride and transition metal dichalcogenides. Widely applied methods¹⁻⁸ include mechanical exfoliation, liquid exfoliation and direct crystal growth approaches such as chemical or physical vapour deposition and molecular beam epitaxy. Two-dimensional materials beyond this library, especially those without known three-dimensional counterparts, remain largely unexplored and new approaches to 2D synthesis and characterization are needed.

In general, the growth of 2D crystals involves the transport of atoms or molecules from the source to the growth area on the substrate. This mass transport process typically occurs in an open space, for example, in a furnace with noble gas carriers in vapour deposition or in a vacuum chamber in molecular beam epitaxy. Alternatively, a liquid metal environment has been used to synthesize 2D metal oxides¹⁰. Recently, a flux-assisted method has also been developed to grow 2D crystals¹¹. In a solid-state environment, mass transport is expected to occur slowly via substitutional or interstitial atomic migration, following Fick's diffusion laws¹², which does not provide an ideal transport mechanism for growing new large-area materials. For instance, recent studies of reactions between metals and transition metal dichalcogenides revealed the formation of new materials only at the interface or in the source's vicinity, within a distance of ~100 nm (refs. 13-15).

¹Department of Physics, Princeton University, Princeton, NJ, USA. ²Department of Chemistry, Princeton University, Princeton, NJ, USA. ³Princeton Materials Institute, Princeton University, Princeton, NJ, USA. Department of Electrical and Computer Engineering, Princeton University, Princeton, NJ, USA. 5Research Center for Electronic and Optical Materials, National Institute for Materials Science, Tsukuba, Japan. 6Research Center for Materials Nanoarchitectonics, National Institute for Materials Science, Tsukuba, Japan. ⁷These authors contributed equally: Yanyu Jia, Fang Yuan.

e-mail: yanyuj@princeton.edu; lschoop@princeton.edu; sanfengw@princeton.edu

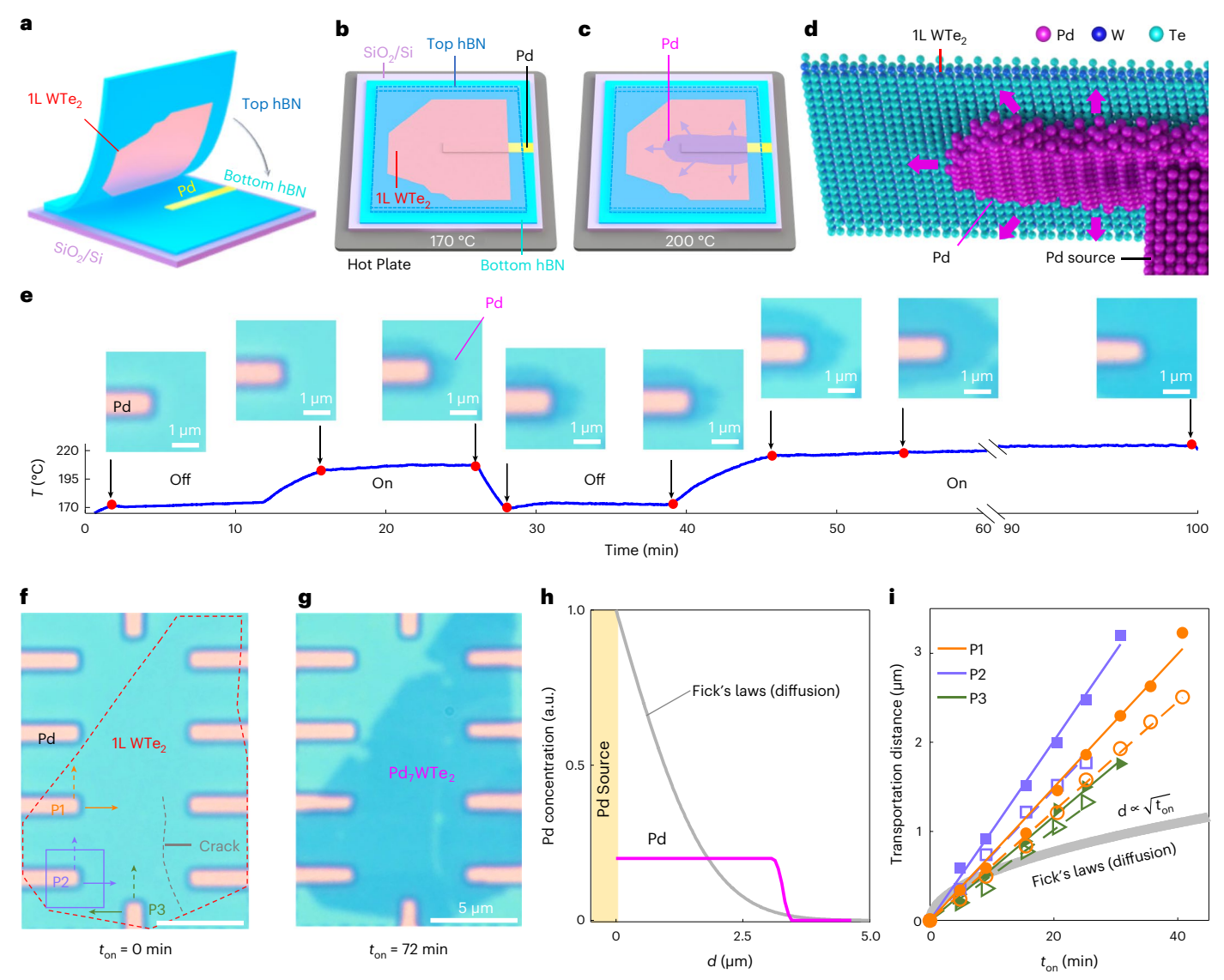


Fig. 1| **Long-distance anomalous mass transport of Pd atoms on monolayer WTe₂. a**, Cartoon illustration of the as-fabricated vdW stacked structure with
monolayer (1L) WTe₂. **b**, **c**, Cartoon illustrations of the observed mass transport
phenomenon on monolayer WTe₂. At 170 °C, no visible change in any of the
materials is observed (**b**), while at 200 °C, clear mass transport is seen (**c**). **d**, Cartoon illustration of the Pd transport process on crystalline monolayer
WTe₂. **e**, Mass transport controlled by modifying the temperature (*T*). The optical
images were taken throughout the process near one of the Pd islands in device
D1 (indicated by the purple square in **f**). The mass transport can be switched
on or off by changing the temperature. **f**, Optical image of device D1 before Pd
transport. The monolayer WTe₂, invisible in this image, is outlined by the red

dashed line. $t_{\rm on}$ is the time that the device is held at a temperature above 190 °C during the process in ${\bf e}$. The three Pd contacts chosen for analysis are labelled P1, P2 and P3. Scale bar, 5 µm. ${\bf g}$, Optical image of the same device after holding the temperature at -200 °C for 72 min. The product 2D crystal Pd₇WTe₂ is now visible as the optically darker region. ${\bf h}$, Illustration of the contrast between the observed concentration profile of Pd with distance (d) in device D1 (based on optical contrast) and the expectation based on Fick's laws. ${\bf i}$, Time-dependent transport distance extracted from the images of device D1. The data points, represented with different shapes and colours, correspond to the distance of transport from Pd contacts P1, P2 and P3 in the directions indicated by the solid and dashed arrows in ${\bf f}$.

Nevertheless, mass transport phenomena and mechanisms through nanoconfined solid structures or surfaces remain largely unexplored, despite their critical importance in a wide range of fields, including molecular biology, nanotechnology and quantum materials science. For instance, studies of ion and molecular transport through a carbon nanotube^{16,17} or an atomically thin nanoslit formed inside a vdW structure^{18,19} have raised many intriguing questions regarding nanofluidics^{20,21}. Interesting possibilities, such as nearly frictionless flow^{18,22}, critical wetting²³, nanoconfined chemistry²⁴ on a 2D crystal and collective phases of atoms adsorbed on a monolayer²⁵, to name a few, await experimental exploration. Here we report the surprising observation of rapid, non-Fickian mass transport of atomically thin metals on monolayer crystals over a very long distance at temperatures

well below the melting points of all the materials involved. As an example, we demonstrate in detail the propagation process and results of 2D Pd film transport on monolayer WTe $_2$. Our experiments establish a generalizable approach, strictly confined in a 2D nanospace near the surface of a monolayer crystal, for the growth of new 2D materials and crystalline structures that are inaccessible by pre-existing methods.

Results

Long-distance mass transport on a monolayer

We started by fabricating a vdW stack (Fig. 1a) in which monolayer WTe $_2$ and predeposited Pd islands (~20 nm thick) were fully encapsulated in chemically inert hexagonal boron nitride (hBN). The monolayer WTe $_2$ was mechanically exfoliated from bulk WTe $_2$ (refs. 26–28), and the Pd

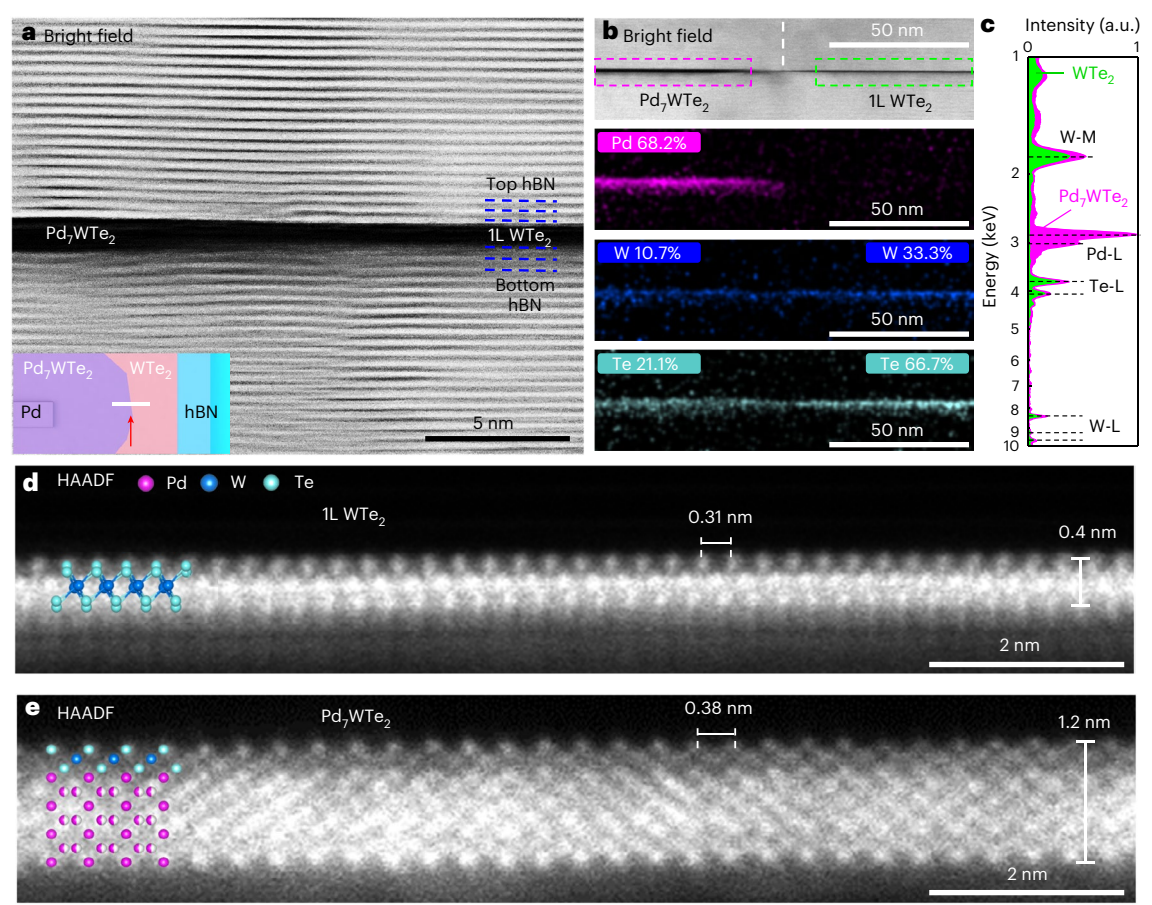


Fig. 2 | **Nanoconfined crystal growth on monolayer WTe₂. a**, A bright-field STEM image (cross-section) obtained at the Pd_7WTe_2 and WTe_2 interface in a vdW stacked device (D2). The position of this image within the stack is indicated by the white bar in the cartoon inset. **b**, EDX analysis of Pd_7WTe_2 (left side) and monolayer WTe_2 (right side) in device D3, showing the elemental composition. The lateral interface is indicated by a white dashed line. **c**, Superimposed EDX spectra of both sides of the stack, of the areas indicated by the dashed boxes in

 $\label{eq:bc} \textbf{b}, corresponding to Pd_7WTe_2 and WTe_2. The characteristic X-ray energy peaks corresponding to electron relaxation to the L/M shell of W and Te, namely, W-M, W-L and Te-L, are well resolved in both areas, while Pd-L peaks emerge only in the Pd_7WTe_2 region. <math display="block"> \textbf{d}, A \ HAADF-STEM \ image \ of \ monolayer \ WTe_2 \ in \ device \ D3. \\ \textbf{e}, A \ HAADF-STEM \ image \ of \ the \ new \ 2D \ crystal line \ structure \ Pd_7WTe_2 \ synthesized on the \ same \ device. Monolayer \ WTe_2 \ and \ proposed \ Pd_7WTe_2 \ crystal \ structures are \ superimposed \ in \ \textbf{d} \ and \ \textbf{e} \ (see \ Extended \ Data \ Fig. 5 \ for \ details).$

islands were created on the bottom hBN substrate using nanolithography and metal deposition techniques. The fully encapsulated vdW stacks were created and placed on top of a 285 nm SiO₂/Si substrate using standard 2D dry transfer techniques in an argon-filled glove box (see Methods, Fig. 1 and Extended Data Fig. 1a). During the transfer process, the entire stack was heated to ~170 °C, at which temperature we observed no visible mass transport phenomena under an optical microscope (Fig. 1b). On heating the vdW stack to above 190 °C, we observed a clear expansion of Pd atoms seeded from the Pd islands underneath WTe₂ (Fig. 1c,d). This is indicated by the optically darker regions in the series of optical microscopy images shown in Fig. 1e, which reveal a continuous, rapid expansion of the dark region over time. Holding the temperature at ~200 °C for ~70 min, we found that the expansion of Pd covers nearly the entire monolayer WTe2 (Fig. 1f,g). The continuous mass-spreading process in device D1 is shown in Supplementary Video 1. Extended Data Fig. 1b shows an atomic force microscopy (AFM) image of the same device, which clearly reveals that, after expansion, the seed Pd islands become thinner and narrower. Near the separated Pd islands not in contact with monolayer WTe₂, no visible change of any material is seen. The expansion stops at the monolayer edge, meaning that no spreading of any material is seen on hBN in the absence of WTe₂.

We highlight here the key features of this unexpected observation. In the standard diffusion process dictated by Fick's laws, the diffusion flux is determined by the concentration gradient, which leads to 12

(1) an exponential decay in the spatial profile of the concentration, c(x), of the diffusive atoms, $c(x) \propto \exp(-x^2/4Dt)$, and (2) a time-dependent diffusion distance, $d(t) \propto \sqrt{t}$, where D is the diffusion coefficient and (x, t) are the space-time coordinates. Both descriptions are invalid in our observations. The spatial distribution of the propagating Pd, as already indicated by the uniform optical contrast in Fig. 1e,g, seems to be of a constant concentration moving away from the seed Pd, sharply dropping to zero at the front. This is in stark contrast to Fickian diffusion, as illustrated in Fig. 1h. The thickness of the uniform ultrathin Pd film spread over the WTe₂ monolayer is ~0.8 nm, as measured by AFM (Extended Data Fig. 2). We also extracted the time-dependent transport distance (Fig. 1i), measured between the moving front and the Pd source along two directions from three sources, P1, P2 and P3, indicated in Fig. 1f. We found a linear time dependence, $d(t) \propto t$, that is, the front propagates at a constant speed, in the order of ~0.1 µm min⁻¹. These features reveal that the unusual mass transport phenomenon observed here is non-Fickian, in other words, non-diffusive. We note that while a similar device geometry has previously been used to study the diffusive and interfacial reactions between Pd and multilayer WTe₂ (refs. 13,14), our finding of non-Fickian rapid mass transport is qualitatively distinct; here, the Pd transport distance is very long and only limited by the size of the seed monolayer, critical for enabling large-area 2D growth.

Indeed, the entire process occurs as if the Pd atoms are flowing over the monolayer WTe₂, like a liquid. The challenge in this picture is

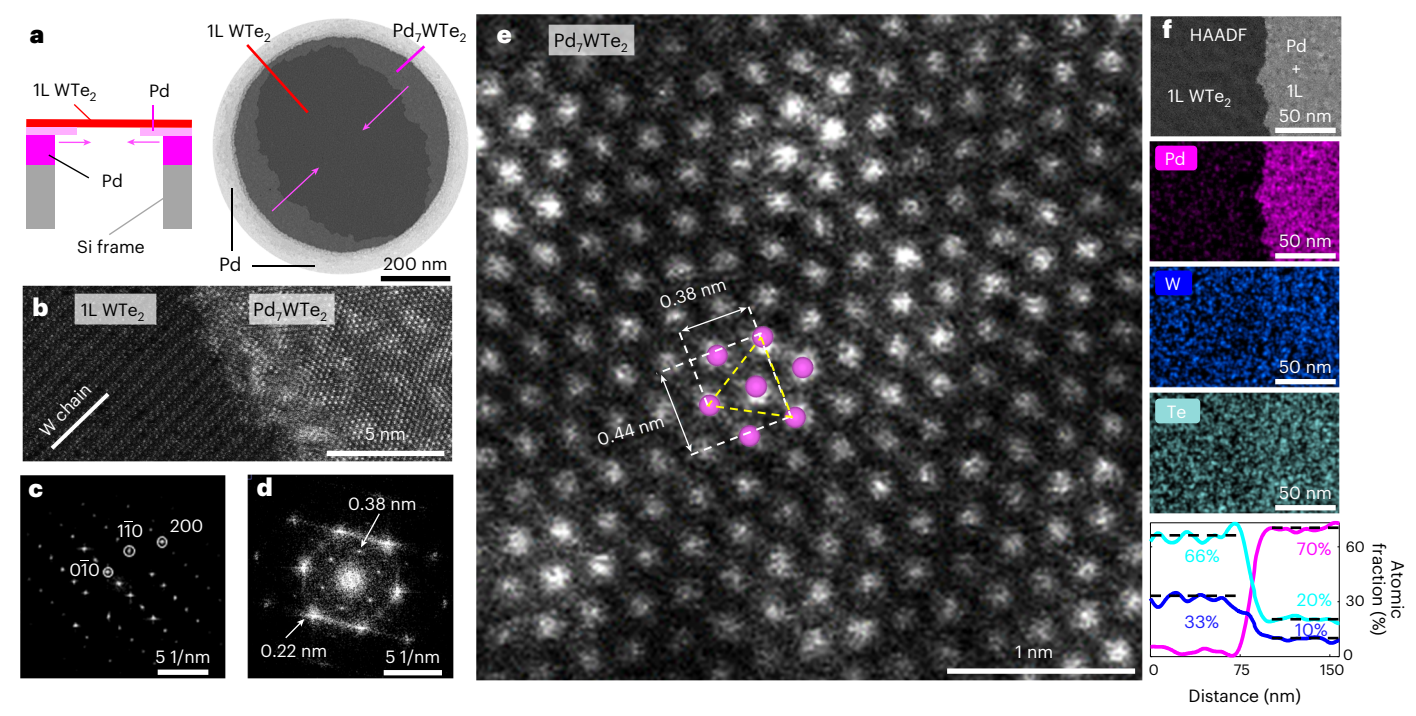


Fig. 3 | **In-plane lattice structure of Pd**₇**WTe**₂, **a**, A cartoon illustration of the structure of a suspended TEM device D4 (left) and its STEM image (right). The grid was coated with Pd, followed by a monolayer of WTe₂ on top. Pd transport was induced by heating the sample above 190 °C, and the new 2D material Pd₇WTe₂ was formed on the suspended WTe₂. Regions of different materials are indicated. **b**, An atomic-resolution STEM image of the interface region of Pd₇WTe₂ and monolayer WTe₂. The direction of the W chain in WTe₂ is indicated. **c**, An FFT

pattern of the monolayer WTe $_2$ crystal with its Miller indices indicated. **d**, An FFT pattern of the Pd $_7$ WTe $_2$ crystal with six-fold symmetry. The characteristic periodicities of 0.38 and 0.22 nm are indicated. **e**, Magnification of the STEM image of the Pd $_7$ WTe $_2$ crystal, revealing its apparent hexagonal lattice. **f**, Elemental mappings and line-profile composition analysis of the suspended TEM sample near the interface between monolayer WTe $_2$ and Pd $_7$ WTe $_2$.

that the melting point of Pd metal is 1,555 °C. We did not observe any obvious melting of the Pd bulk islands at the temperatures used here. Nevertheless, the fact that the Pd transport can be switched on and off (Fig. 1e) by slightly modifying the temperature suggests the presence of a critical temperature (~190 °C) and that some sort of structural phase transition still occurs. Interestingly, it is known that the melting point of many nanoscale metals can be substantially depressed compared with their bulk value²⁹. We thus suspect that the surface layer of Pd that directly contacts with WTe₂ might melt or undergo a structural transition. Another important aspect relates to the thickness of the spreading Pd film, which seems to be highly uniform (~0.8 nm) and is the same in all samples (Extended Data Fig. 2). At this stage, we do not know what determines this exact thickness, but would like to mention that the interesting theoretical idea of 'critical wetting' on a monolayer crystal²³ may be considered. It is possible that, above 190 °C, we have realized an atomically thin 2D liquid metal (perhaps a partial Pd layer), a highly unusual form of matter not realized previously. Future efforts that combine experiments and theory are necessary to fully understand the exact mechanism of such anomalous non-Fickian mass transport. Importantly, the phenomenon observed here immediately implies new possibilities for growing 2D materials.

Surface-nanoconfined two-dimensional growth on a monolayer

The direct chemical consequence of the Pd transport is the growth of a new 2D material converted from the precursor monolayer (WTe $_2$). We performed high-resolution scanning transmission electron microscopy (STEM) studies on the vdW stack to uncover its atomic structure (see Methods). All the STEM data were collected at room temperature, under which condition the material structure is in a solid phase and is stable (that is, there is no active Pd transport). Figure 2a shows a bright-field

STEM image of the stack (cross-section view) at a selected location near the Pd front, where we see both the Pd-covered area and the bare WTe₂ monolayer (Fig. 2a, inset). The new material is clearly thicker than the monolayer, consistent with the darker appearance observed by optical microscopy (Fig. 1) and AFM measurements (Extended Data Fig. 2). The image immediately confirms the extremely sharp Pd front, with a lateral interface of only ~5 nm at the transition (Fig. 2a). Energy-dispersive X-ray spectroscopy (EDX) revealed the dominant presence of Pd atoms in the new structure on the left side of the stack, while no Pd was found on the right side (Fig. 2b,c). In contrast, W and Te atoms are present on both sides in a composition ratio of 1:2, as expected. In the new material region shown in Fig. 2b, the atomic ratio of Pd/W/Te was found to be 68.2:10.7:21.1, very close to 7:1:2. A systematic EDX analysis at different locations revealed a similar atomic ratio close to 7:1:2 in each case (Extended Data Figs. 3 and 4). Hence, we attribute to this new 2D material structure a nominal chemical formula of Pd₇WTe₂.

Remarkably, this new material exhibits a crystalline structure, as revealed in the high-angle annular dark field (HAADF) STEM measurements. The HAADF-STEM cross-section image of the pristine WTe $_2$ monolayer region in device D3 (Fig. 2d) shows the expected lattice structure. Figure 2e presents a HAADF-STEM image of the Pd $_7$ WTe $_2$ region in the same device, which interestingly uncovers a crystalline structure that is qualitatively different from the neighbouring WTe $_2$ monolayer. The new structure, dominated by Pd atoms, arranges compactly in 2D form. We suspect that the W and Te atoms remain bonded and are located on the top of the stack, as evidenced by the slightly darker top three layers in Fig. 2e. Our experiments, unfortunately, were not able to distinguish the atom species site by site, and hence the confirmation of its structure requires future studies. A lateral interatomic spacing of 0.38 nm is observed in the side-view image of Pd $_7$ WTe $_2$, noticeably larger than the 0.31 nm observed in the pristine WTe $_2$, which indicates

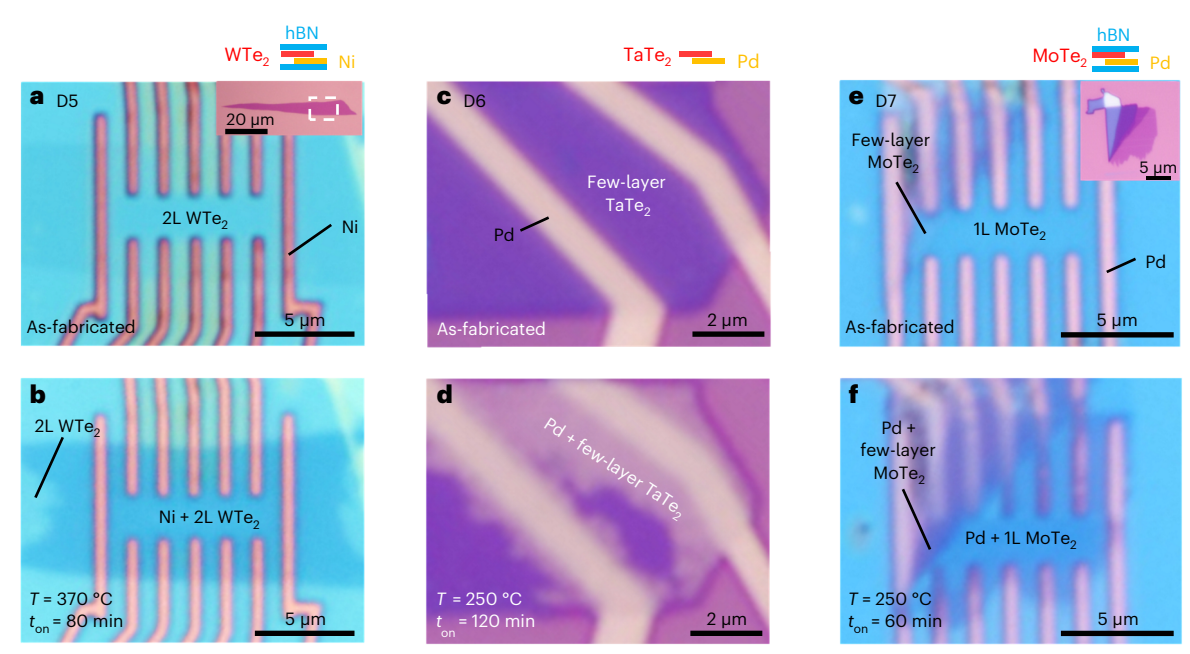


Fig. 4 | **Generalization of the unusual mass transport. a**, Optical image of device D5 with bilayer (2L) WTe₂ and Ni sources encapsulated by hBN before thermal treatment. Inset: as-exfoliated bilayer WTe₂ and the white dashed box indicates the area of WTe₂ visualized in the main panel. The stack structure is shown above the figure. **b**, Optical image of the same device after being held at -370 °C for 80 min. Ni transport was induced on and only on WTe₂, visualized as the optically darker region. The critical temperature to turn on Ni transport on bilayer WTe₂ is 350 °C; the stack was held at a slightly higher temperature (370 °C) to speed up the process. **c**, Optical image of device D6 with few-layer TaTe₂ and Pd contacts,

as fabricated. The stack structure is shown above the figure. $\bf d$, Optical image of the same device after being held at 250 °C for 120 min. The colour of TaTe₂ changed from purple to yellow on heating, which indicates the transport of Pd and formation of new materials. $\bf e$, Optical image of device D7 with both monolayer and few-layer MoTe₂ and Pd contacts. Image: an as-exfoliated MoTe₂ flake. The stack structure is shown above the figure. $\bf f$, Optical image of the same device after being held at 250 °C for 60 min. The colour of both monolayer and few-layer MoTe₂ became darker due to Pd transport. We observed similar Pd transport behaviours on both 2H and 1T′ phases of MoTe₂ (the image shown here is the 1T′ phase).

a structural change of WTe $_2$ inside Pd $_7$ WTe $_2$. Comparison of these distances with those observed in elemental bulk Pd (Extended Data Fig. 5) revealed clear differences. We note that the process observed here is distinguished from vdW epitaxy 30 as we did not observe a van der Waals gap between the Pd and W–Te layers.

To visualize the in-plane atomic structure of this new 2D crystal, we prepared another sample on a standard transmission electron microscope (TEM) grid (see Methods), where the monolayer is fully suspended over the holes. Pd was predeposited on the frame of the TEM grid (Fig. 3a) and no hBN was used to ensure the exposure of the target crystal. Using the same heating procedure, Pd transport was induced on the suspended WTe₂ and the new crystal was formed. This observation further confirms the mass transport of Pd on WTe₂ and that hBN is not essential (although the use of hBN stacks could improve the quality of the new crystal). Figure 3b shows a high-resolution HAADF-STEM image (plan view) at the boundary between monolayer WTe₂ and Pd₇WTe₂; both materials can be resolved with atomic resolution. The direction of the zigzag W chain of monolayer WTe₂ is indicated. Fast Fourier transformation (FFT) of the monolayer WTe2 area yielded its characteristic diffraction pattern (Fig. 3c), consistent with its rectangular unit cell and strong lattice anisotropy. The high-resolution STEM image of the Pd₇WTe₂ region shows a qualitatively different crystal structure, whose FFT pattern (Fig. 3d) displays a six-fold symmetric pattern that is absent in WTe₂. Indeed, a magnified view of the Pd₇WTe₂ lattice shows an apparent hexagonal lattice (Fig. 3e). The characteristic interatomic length of 0.38 nm observed in the cross-section image in Fig. 2e can also be identified here (Fig. 3e). We also performed EDX analysis on these suspended TEM devices, which again revealed a Pd/W/Te atomic composition of 7:1:2, the same as in the hBN-encapsulated samples (Fig. 3f).

These observations also confirmed that the same crystalline structure of Pd₇WTe₂ was obtained for the two types of growth (hBN-encapsulated growth and suspended growth). Specifically, both samples were fabricated on monolayer WTe $_2$, the W and Te atoms were of the same density, and the same atomic composition determined by EDX confirmed that the 2D Pd density is the same for both growth types. Furthermore, the Pd on both films shows a crystalline structure with an identical lattice constant (the interatomic distance of 0.38 nm). Based on these observations, we propose a unique atomic structural model for the new material Pd $_7$ WTe $_2$ (see Methods and Extended Data Fig. 5). To the best of our knowledge, neither the unusual hexagonal form of the 2D Pd layer nor a crystalline Pd $_7$ WTe $_2$ structure has been reported previously.

We further note that the as-grown Pd_7WTe_2 is highly uniform over the entire area defined by the seed monolayer WTe_2 . Extended Data Fig. 6 confirms the uniform thickness of Pd_7WTe_2 over a large area (micrometres), directly based on atomic-scale STEM measurements, and Extended Data Fig. 7 shows that the lattice orientation of Pd_7WTe_2 is determined by the seed monolayer WTe_2 , as revealed by STEM analysis of the Pd front at various locations on the single monolayer, separated by large distances. Thus, the crystal orientation of the as-grown Pd_7WTe_2 is locked to the crystal direction of the single-crystalline WTe_2 monolayer seed.

Generalization of the mass transport

We next explored whether this phenomenon of 2D crystal growth within a nanoconfined 2D space on an atomically thin crystal is unique to Pd on WTe₂ or whether it is generalizable. First, we investigated the behaviour of Pd on bilayer WTe₂ and observed that similar Pd transport occurs (see Methods and Extended Data Figs. 2 and 8–10). We found that the thickness of the material synthesized from bilayer WTe₂ is twice that synthesized from a monolayer, with the same atomic composition (Pd₇WTe₂). STEM analysis revealed a hexagonal lattice consistent with monolayer Pd₇WTe₂ in some regions of the bilayer-seeded sample. Yet, we also observed other structures and domains, including moiré

patterns (Extended Data Fig. 10). This is distinct from the growth on the monolayer, where we found a highly uniform structure over a very large area. Future experiments are required to fully characterize the bilayer-seeded growth, which may yield interesting possibilities, including the potential creation of new moiré materials.

Figure 4 illustrates three additional examples of mass transport. The first is the observation of a similar long-distance transport of nickel on bilayer WTe₂ at a temperature of ~370 °C, again well below the known melting point of Ni (1,455 °C). This can be clearly visualized by the change in colour of the optical images of the vdW stack under a microscope after the thermal treatment (Fig. 4a,b). The second is a similar transport of Pd on few-layer TaTe, at a temperature of ~250 °C (Fig. 4c,d). Here, the optical contrast of the resulting material using a few-layer flake is brighter than that of monolayer- or bilayer-seeded samples, indicating that more Pd transports into the few-layer samples. In the third example, Pd transports similarly along a monolayer MoTe₂ (Fig. 4e,f), with the Pd residing on the entire flake after the vdW stack is held at 250 °C for 60 min. It seems that all these observations involve melting point depression²⁹ of nanoscale metals, reactive 2D interfaces and chemical interactions. The non-Fickian transport characteristics (Fig. 1) imply that simple diffusion cannot explain these observations and we believe that chemical affinity plays a key role. Future efforts are necessary to identify the exact mechanism of the anomalous mass transport in the various cases reported here. This understanding may provide new insights into nanoscale atomic transport. If the transporting metal is indeed partially in a liquid phase, then our experiments have realized an atomically thin 2D liquid metal, a highly intriguing situation that was previously unknown. Overall, our results imply that the anomalous non-Fickian transport phenomenon is, surprisingly, ubiquitous for various metals on existing 2D crystals.

Summary

This work demonstrates a route for controlled chemistry on a monolayer. We envision that the nanoconfined growth mechanism templated on monolayer crystals will greatly expand the library of 2D materials ^{1,2,9} and their functionalities, especially as it represents a strategy for synthesizing 2D materials inaccessible using conventional approaches. In contrast to conventional 2D growth techniques, the approach reported here is highly compatible with existing mature techniques for creating high-quality 2D devices, including vdW encapsulation and nanodevice fabrication, a big advantage for further engineering and investigating their physical properties and device functionalities. Exploration along these lines may enable advances in the study of 2D superconductors, magnets and topological states of matter.

Methods

Device fabrication

vdW stacks. High-quality WTe $_2$ bulk crystals were grown according to previously described methods^{28,31}. The flux-grown crystals were synthesized by a solid-state reaction using Te as the flux. Te (99.9999%, Alfa Aesar) and W (99.9%, Sigma-Aldrich) were mixed in a molar ratio of 98.8:1.2 and then sealed in an evacuated quartz ampoule, which was heated to 1,020 °C over a period of 16 h. The mixture was then slowly cooled to 700 °C at a rate of 1.2 °C h $^{-1}$ and then to 540 °C at a rate of 2 °C h $^{-1}$. The crystals were obtained by a decanting procedure in a centrifuge.

To prepare the vdW stacks, hBN flakes were exfoliated on $\rm SiO_2/Si$ substrates and identified under an optical microscope. hBN flakes of appropriate thickness (7–23 nm) were characterized by AFM before being transferred onto undoped $\rm SiO_2/Si$ wafers with prepatterned metal alignment markers using standard dry transfer techniques. We then used electron beam lithography, followed by cold development, reactive ion etching and metal deposition to deposit the patterned Pd (Ni for device D5) sources (typically 10–20 nm thick, occasionally

with an additional ~3 nm Ti as a sticking layer) on the hBN flakes (except for device D6, whose metal source was directly deposited on SiO $_2$ /Si). These prepared bottom stacks were then cleaned with an atomic force microscope tip. The WTe $_2$ monolayers were exfoliated on SiO $_2$ /Si substrates and identified under an optical microscope in a glove box. Then, hBN and WTe $_2$ were stacked together and subsequently placed on the designated area of the prepared bottom stacks using standard dry transfer techniques. A similar device fabrication procedure can be found in our previous reports ^{27,28}. The final vdW stacks were then placed on a hot plate to induce Pd transport while being monitored under an optical microscope. The whole process involving WTe $_2$ was performed in a glove box with ambient H $_2$ O < 0.1 ppm and O $_2$ < 0.1 ppm. A similar process was used to create devices with different seed material (TaTe $_2$ and MoTe $_2$) and metal (Ni).

Specifically, device D1 comprised a top hBN layer (7 nm), monolayer WTe $_2$ precursor, a Pd metal source and a bottom hBN layer (23 nm). Device D2 comprised a top hBN layer (10 nm), monolayer and bilayer WTe $_2$ precursor, a Pd metal source and a bottom hBN layer (9 nm). Device D3 comprised a top hBN layer (23 nm), monolayer and few-layer WTe $_2$ precursor, a Pd metal source and a bottom hBN layer (22 nm). Device D4 comprised monolayer WTe $_2$ precursor and a Pd metal source. Device D5 comprised a top hBN layer (-15 nm), bilayer WTe $_2$ precursor, a Ni metal source and a bottom hBN layer (12 nm). Device D6 comprised a few-layer TaTe $_2$ precursor and a Pd metal source. Device D7 comprised a top hBN layer (-13 nm), monolayer and few-layer MoTe $_2$ precursor, a Pd metal source and a bottom hBN layer (18 nm).

TEM cross-section devices. TEM cross-section devices were created starting with the vdW stacks produced by the above method. After Pd transport, the stacks were sputter-coated with 50-nm-thick amorphous carbon as a protective layer before being loaded into a Helios NanoLab G3 UC dual-beam focused ion beam scanning electron microscope (FIB-SEM) system. Next, a lamella specimen was cut out from the stack by a standard lift-out process within the FIB-SEM system, transferred onto a TEM grid and its cross-section polished until electron transparent (thickness -50 nm). Samples were thinned by gently polishing the sample using a 2 kV Ga⁺ ion beam to minimize surface damage caused by the ion beam. Finally, the specimen was quickly transferred into a TEM for high-resolution imaging.

Suspended TEM devices. Standard TEM grids with holey silicon nitride support film were first treated with oxygen plasma for 5 min on both sides and then 20 nm Pd was deposited onto the grids. Next, WTe $_2$ monolayers were exfoliated and transferred onto the TEM grids using standard dry transfer techniques. The grids, covered with WTe $_2$ and a layer of polycarbonate used for the transfer process, were then placed on a hot plate with the temperature maintained at -190 °C for 5 min. The polycarbonate was then removed by immersing the grids in chloroform for 1 h in a glove box. The TEM grids were then mounted onto a Gatan double tilt vacuum transfer holder. The exfoliation, stacking, crystal growth, polycarbonate removal and sample mounting were all performed in a glove box with ambient H $_2$ O < 0.1 ppm and O $_2$ < 0.1 ppm. The devices were also well protected from air by the vacuum transfer holder (filled with Ar) when it was transferred from the glove box to the TEM instrument.

Optical and AFM measurements

The optical measurements were carried out using a home-built transfer set-up with a hot plate, Nikon Eclipse LV150N microscope and Canon EOS 5D Mark IV DSLR camera. The video shown in Supplementary Video 1 was recorded using OBS Studio software and edited with VideoProc Vlogger. The optical images displayed in this report were either directly captured by the camera or extracted from the recorded video. The AFM data were obtained with either a Bruker Dimension Edge or Bruker Dimension Icon microscope and analysed with the NanoScope Analysis software.

Microstructure characterization

Atomic-resolution HAADF-STEM imaging and EDX mapping were performed on a Titan Cubed Themis 300 double Cs-corrected scanning/transmission electron microscope equipped with an extreme field emission gun source and a super-X EDS system. The system was operated at 300 kV.

Atomic modelling of the new 2D material Pd₇WTe₂

As the new material was Pd rich, we first compared its STEM image with the lattice of crystalline, elemental Pd. The face-centred cubic structure of Pd displays a hexagonal lattice when viewed along both the [111] and [110] directions. Along the [111] direction, equilateral hexagonal lattices are close-packed with an A-B-C-A stacking order (Extended Data Fig. 5a.b: in the plots. Pd atoms in different layers are coloured differently to illustrate the stacking order). The interatomic spacing in crystalline Pd along the [111] direction is noticeably smaller than that in Pd₇WTe₂ (0.275 nm compared with 0.44 nm). Indeed, we simulated the diffraction pattern of atomically thin Pd viewed along the [111] direction, and it is clearly different from the experimentally observed diffraction pattern of Pd₇WTe₂ (Fig. 3d). Viewed along the [110] direction, the structure of Pd consists of stacked rectangular lattices with an A-B-A stacking order, resulting in a distorted hexagonal lattice (Extended Data Fig. 5c,d). The distorted hexagon is further revealed in the simulated diffraction pattern, which shows different periodicities (0.19 and 0.22 nm) along two high-symmetry directions. While the observed interatomic distance in this arrangement is much closer to the measured value in Pd₇WTe₂ (0.389 versus 0.38 nm), the symmetry of the pattern does not satisfactorily describe that of Pd₇WTe₂, which maintains a six-fold symmetry (Fig. 3d). Thus, it seems that the Pd lattice observed within Pd₇WTe₂ (in plan view) resembles a substantially strained Pd [111] lattice, equivalent to ~60% strain. This is dramatically greater than in other reported strained Pd nanocrystals, such as the Pd islands found in PdCoO₂ (~4% strain)³².

From the data collected in this study, we can propose a model to describe the observed Pd_7WTe_2 lattice structure. The plan and cross-section views of the proposed crystal structure for Pd_7WTe_2 are shown in Extended Data Fig. 5e,f. The material consists of ten atomic layers, each with a hexagonal lattice with a lattice constant of 0.44 nm. In the vertical direction, the ten atomic layers are close-packed. In the model, we assume that the top three layers are Te-W-Te, also arranged in a hexagonal lattice (like the Te-W-Te), with a stacking order of Te-W-Te. The bottom seven layers are occupied by Te-W-Te and stacked in an Te-W-Te (where Te-W-Te). All characteristic lengths, in both the top and side views, are consistent with the observations presented in Figs. 2 and 3. The simulated diffraction pattern also agrees with our experimental diffraction pattern (Fig. 3d). More details of the model may be resolved in future experiments.

Pd transport on bilayer WTe₂

Pd transport process. The transport of Pd on bilayer WTe₂ was investigated using device D2, which contained both mono- and bilayer WTe₂ regions as well as separated Pd sources. The transport process is illustrated in the optical images shown in Extended Data Fig. 8. Two notable effects were observed during the process: (1) Pd spreads on the bilayer at a lower critical temperature (-170 °C) than on the monolayer (-190 °C; Extended Data Fig. 8c) and (2) an interesting 'diode effect' is observed in the propagation of Pd across the monolayer–bilayer step, that is, Pd can freely transport from the monolayer to the bilayer, but not in the reverse direction, as illustrated in Extended Data Fig. 8d. We do not currently fully understand these interesting observations.

Bilayer-seeded Pd₇**WTe**₂. The thickness of the material resulting from Pd transport on bilayer WTe₂ was measured to be -3.1 nm by AFM (Extended Data Fig. 2), which is twice the thickness of Pd₇WTe₂ on

monolayer WTe₂ (~1.5 nm by AFM). This double thickness effect was further confirmed by the HAADF-STEM cross-section images of bilaver WTe₂ (spot S1) and the resulting material (spot S2, Extended Data Fig. 9). EDX analysis of both cross-section and plan-views (Extended Data Figs. 9d and 10e, respectively) confirmed the same atomic ratio of Pd/W/Te, close to 7:1:2, as for the monolayer-seeded Pd₇WTe₂. The in-plane lattice structure of the bilayer-seeded Pd₇WTe₂ is shown in Extended Data Fig. 10. In some regions, we found a crystalline structure consistent with the hexagonal lattice of the monolayerseeded Pd₇WTe₂ (Extended Data Fig. 10a), but we also found regions that display other patterns, including moiré patterns (Extended Data Fig. 10b-d). This contrasts with monolayer-seeded samples, where we typically found a uniform crystalline structure. The inhomogeneity of the bilayer-seeded suspended sample may be caused during the fabrication process. Further experiments are necessary to fully understand the bilayer-seeded growth.

Data availability

All data supporting the findings of this study are available in the main text. Source data are provided with this paper.

References

- Geim, A. K. & Grigorieva, I. V. Van der Waals heterostructures. Nature 499, 419–425 (2013).
- Novoselov, K. S., Mishchenko, A., Carvalho, A. & Castro Neto, A. H.
 materials and van der Waals heterostructures. Science 353, aac9439 (2016).
- 3. Liu, Y., Huang, Y. & Duan, X. Van der Waals integration before and beyond two-dimensional materials. *Nature* **567**, 323–333 (2019).
- Cai, Z., Liu, B., Zou, X. & Cheng, H.-M. Chemical vapor deposition growth and applications of two-dimensional materials and their heterostructures. *Chem. Rev.* 118, 6091–6133 (2018).
- Andrei, E. Y. et al. The marvels of moiré materials. Nat. Rev. Mater.
 Q01–206 (2021).
- 6. Zhou, J. et al. A library of atomically thin metal chalcogenides. *Nature* **556**, 355–359 (2018).
- Wu, S. et al. Vapor-solid growth of high optical quality MoS₂ monolayers with near-unity valley polarization. ACS Nano 7, 2768–2772 (2013).
- Huang, C. et al. Lateral heterojunctions within monolayer MoSe₂–WSe₂ semiconductors. Nat. Mater. 13. 1096–1101 (2014).
- Mounet, N. et al. Two-dimensional materials from high-throughput computational exfoliation of experimentally known compounds. *Nat. Nanotechnol.* 13, 246–252 (2018).
- 10. Zavabeti, A. et al. A liquid metal reaction environment for the room-temperature synthesis of atomically thin metal oxides. *Science* **358**, 332–335 (2017).
- 11. Zhang, P. et al. Flux-assisted growth of atomically thin materials. *Nat. Synth.* **1**, 864–872 (2022).
- 12. Philibert, J.-M. Atom Movements—Diffusion and Mass Transport in Solids (EDP Sciences, 2012).
- Endres, M. et al. Transparent Josephson junctions in higher-order topological insulator WTe₂ via Pd diffusion. *Phys. Rev. Mater.* 6, L081201 (2022).
- Ohtomo, M. et al. Josephson junctions of Weyl semimetal WTe₂ induced by spontaneous nucleation of PdTe superconductor. *Appl. Phys. Express* 15, 075003 (2022).
- Wu, Y. et al. Synthesis of superconducting two-dimensional nonlayered PdTe by interfacial reactions. *Nat. Synth.* 1, 908–914 (2022).
- Hummer, G., Rasaiah, J. C. & Noworyta, J. P. Water conduction through the hydrophobic channel of a carbon nanotube. *Nature* 414, 188–190 (2001).
- Secchi, E. et al. Massive radius-dependent flow slippage in carbon nanotubes. Nature 537, 210–213 (2016).

- Nair, R. R., Wu, H. A., Jayaram, P. N., Grigorieva, I. V. & Geim, A. K. Unimpeded permeation of water through helium-leak-tight graphene-based membranes. Science 335, 442–444 (2012).
- Yang, Q. et al. Capillary condensation under atomic-scale confinement. *Nature* 588, 250–253 (2020).
- Bocquet, L. & Charlaix, E. Nanofluidics, from bulk to interfaces. Chem. Soc. Rev. 39, 1073–1095 (2010).
- 21. You, Y. et al. Angstrofluidics: walking to the limit. *Annu. Rev. Mater.* Res. **52**, 189–218 (2022).
- Holt, J. K. et al. Fast mass transport through sub-2-nanometer carbon nanotubes. Science 312, 1034–1037 (2006).
- Sengupta, S., Nichols, N. S., Del Maestro, A. & Kotov, V. N. Theory of liquid film growth and wetting instabilities on graphene. *Phys. Rev. Lett.* 120, 236802 (2018).
- Grommet, A. B., Feller, M. & Klajn, R. Chemical reactivity under nanoconfinement. Nat. Nanotechnol. 15, 256–271 (2020).
- Del Maestro, A., Wexler, C., Vanegas, J. M., Lakoba, T. & Kotov, V. N. A perspective on collective properties of atoms on 2D materials. Adv. Electron. Mater. 8, 2100607 (2022).
- Ali, M. N. et al. Large, non-saturating magnetoresistance in WTe₂. Nature 514, 205–208 (2014).
- Wang, P. et al. Landau quantization and highly mobile fermions in an insulator. *Nature* 589, 225–229 (2021).
- 28. Jia, Y. et al. Evidence for a monolayer excitonic insulator. *Nat. Phys.* **18**, 87–93 (2022).
- 29. Allen, G. L., Bayles, R. A., Gile, W. W. & Jesser, W. A. Small particle melting of pure metals. *Thin Solid Films* **144**, 297–308 (1986).
- Koma, A. Van der Waals epitaxy for highly lattice-mismatched systems. J. Cryst. Growth 201-202, 236-241 (1999).
- Ali, M. N. et al. Correlation of crystal quality and extreme magnetoresistance of WTe₂. Europhys. Lett. 110, 67002 (2015).
- 32. Podjaski, F. et al. Rational strain engineering in delafossite oxides for highly efficient hydrogen evolution catalysis in acidic media. *Nat. Catal.* **3**, 55–63 (2019).

Acknowledgements

This work was mainly supported by ONR through a Young Investigator Award (N00014-21-1-2804) to S.W. STEM measurements and device fabrication were supported by NSF through a CAREER award (DMR-1942942) to S.W. and the Materials Research Science and Engineering Center (MRSEC) programme of the National Science Foundation (DMR-2011750) through support to L.M.S. and S.W. Device fabrication was partially supported by the AFOSR Young Investigator programme (FA9550-23-1-0140) to S.W. S.W. and L.M.S. acknowledge support from the Eric and Wendy Schmidt Transformative Technology Fund at Princeton. L.M.S. acknowledges support from the Gordon and Betty Moore Foundation (grant no. GBMF9064), the David and Lucile Packard Foundation and the Sloan Foundation. Y.J. acknowledges support from the Princeton Charlotte Elizabeth Procter Fellowship programme. T.S. acknowledges support from the Princeton Physics Dicke Fellowship programme. A.J.U. acknowledges support from the

Rothschild Foundation and the Zuckerman Foundation. The authors acknowledge the use of Princeton's Imaging and Analysis Center, which is partially supported by the Princeton Center for Complex Materials, a National Science Foundation MRSEC programme (DMR-2011750). K.W. and T.T. acknowledge support from the JSPS KAKENHI (grant nos. 20H00354, 21H05233 and 23H02052) and the World Premier International Research Center Initiative, MEXT, Japan.

Author contributions

Y.J. and S.W. co-discovered the phenomena. Y.J. fabricated all the devices, performed optical and transport measurements, and analysed data, assisted by Y.T., G.Y., T.S., P.W., A.J.U.-N. and M.O. and supervised by S.W. Y.J. and F.Y. co-developed the fabrication and STEM measurement procedures, supervised by L.M.S. and S.W., in collaboration with G.C. and N.Y. R.S. and L.M.S. grew and characterized bulk WTe₂ crystals. K.W. and T.T. provided hBN crystals. S.W. and Y.J. interpreted the results and wrote the paper with input from all authors.

Competing interests

The authors declare no competing interests.

Additional information

Extended data is available for this paper at https://doi.org/10.1038/s44160-023-00442-z.

Supplementary information The online version contains supplementary material available at https://doi.org/10.1038/s44160-023-00442-z.

Correspondence and requests for materials should be addressed to Yanyu Jia, Leslie M. Schoop or Sanfeng Wu.

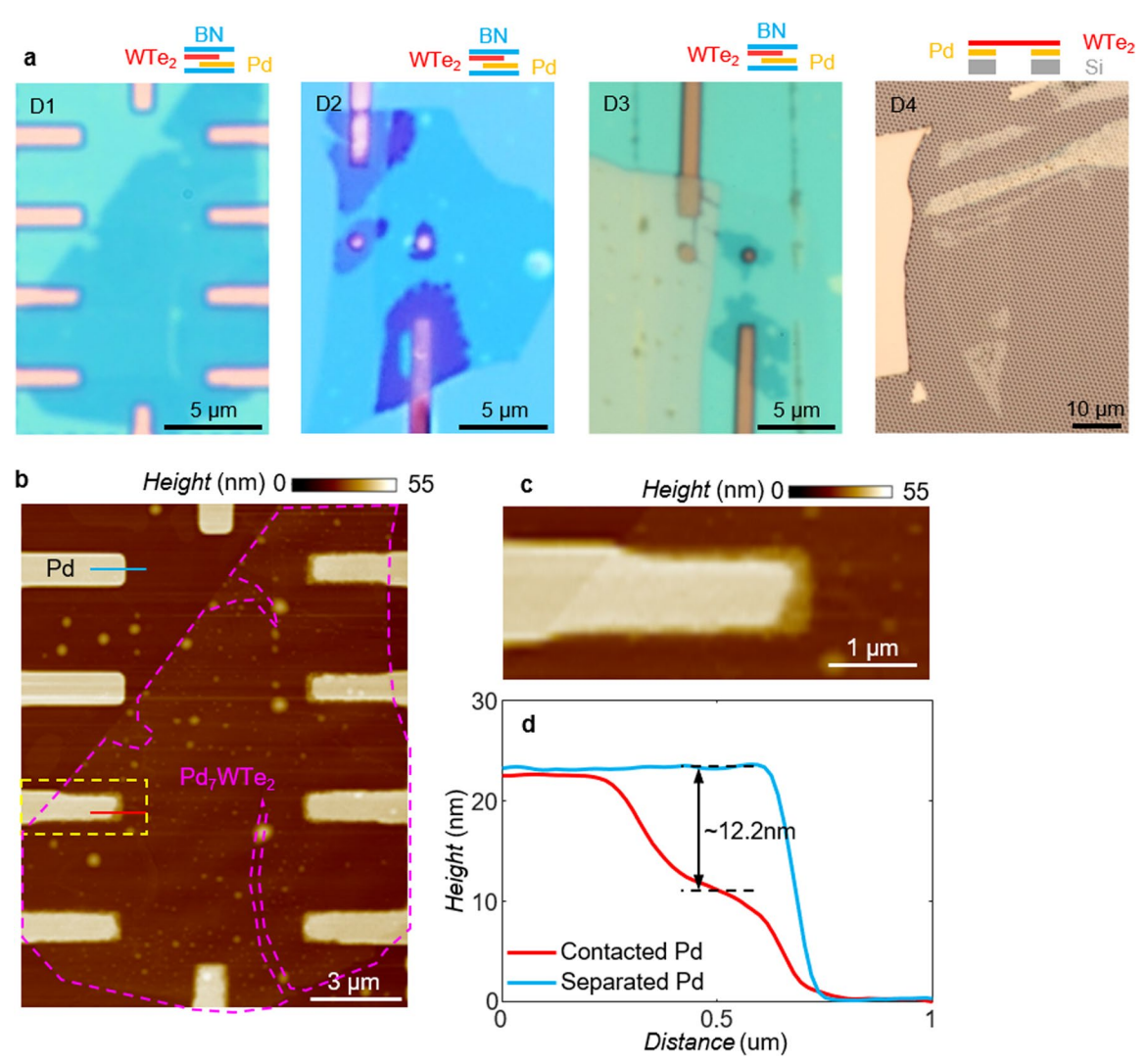
Peer review information *Nature Synthesis* thanks the anonymous reviewers for their contribution to the peer review of this work. Primary Handling Editor: Peter Seavill, in collaboration with the *Nature Synthesis* team.

Reprints and permissions information is available at www.nature.com/reprints.

Publisher's note Springer Nature remains neutral with regard to jurisdictional claims in published maps and institutional affiliations.

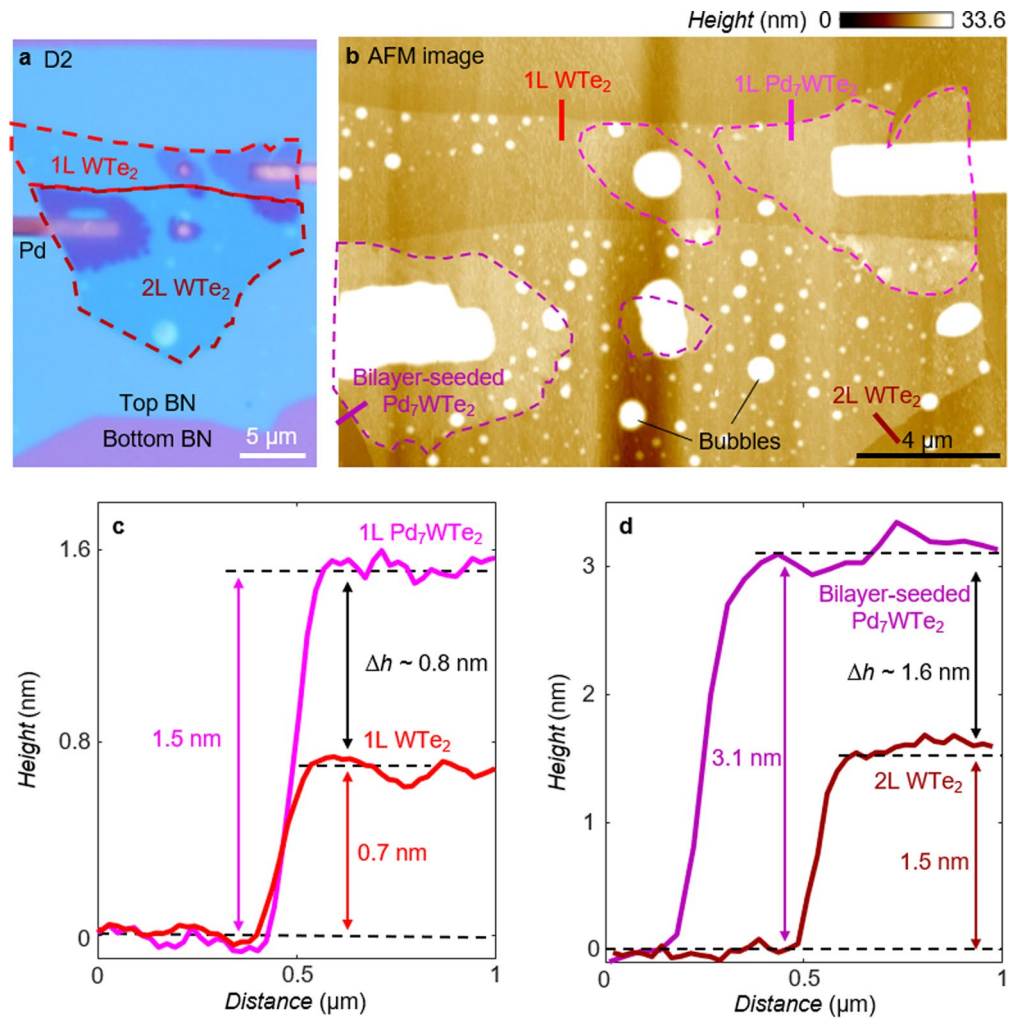
Springer Nature or its licensor (e.g. a society or other partner) holds exclusive rights to this article under a publishing agreement with the author(s) or other rightsholder(s); author self-archiving of the accepted manuscript version of this article is solely governed by the terms of such publishing agreement and applicable law.

@ The Author(s), under exclusive licence to Springer Nature Limited 2023



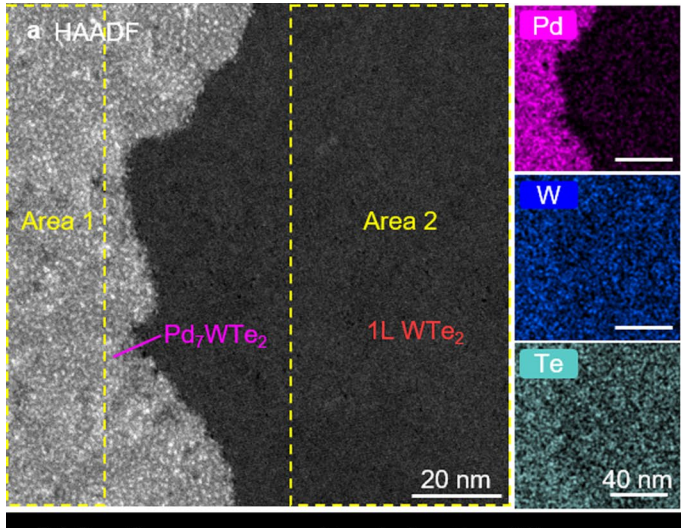
Extended Data Fig. 1 | **Images of devices and AFM characterization of D1 after Pd transport. a.** Optical images of Pd₇WTe₂ devices D1-D4 used in this study are summarized here. Schematic diagrams of the structure of each device (before growth) are sketched next to the image. **b**, The AFM height image, with Pd₇WTe₂

crystal outlined in purple. The Pd islands covered by WTe $_2$ become narrower and thinner, while no visible change is seen for the separated Pd islands. **c**, A zoomedin image of a Pd island, highlighted by the yellow dash line in **b**. **d**, Height profiles of the Pd islands along the indicated lines in **b**.



Extended Data Fig. 2 | **Optical and AFM characterizations of D2. a**, An optical image of D2 after Pd transport. **b**, An AFM height image of D2 with Pd $_7$ WTe $_2$ outlined in purple dash lines. The locations of height profiles measured in **c**,**d** are

indicated by solid lines. \mathbf{c} , The height profile of monolayer WTe₂ and Pd₇WTe₂. \mathbf{d} , The height profile of bilayer WTe₂ and bilayer-seeded Pd₇WTe₂. The height of the bilayer-seeded Pd₇WTe₂ is twice that of the monolayer-seeded Pd₇WTe₂.



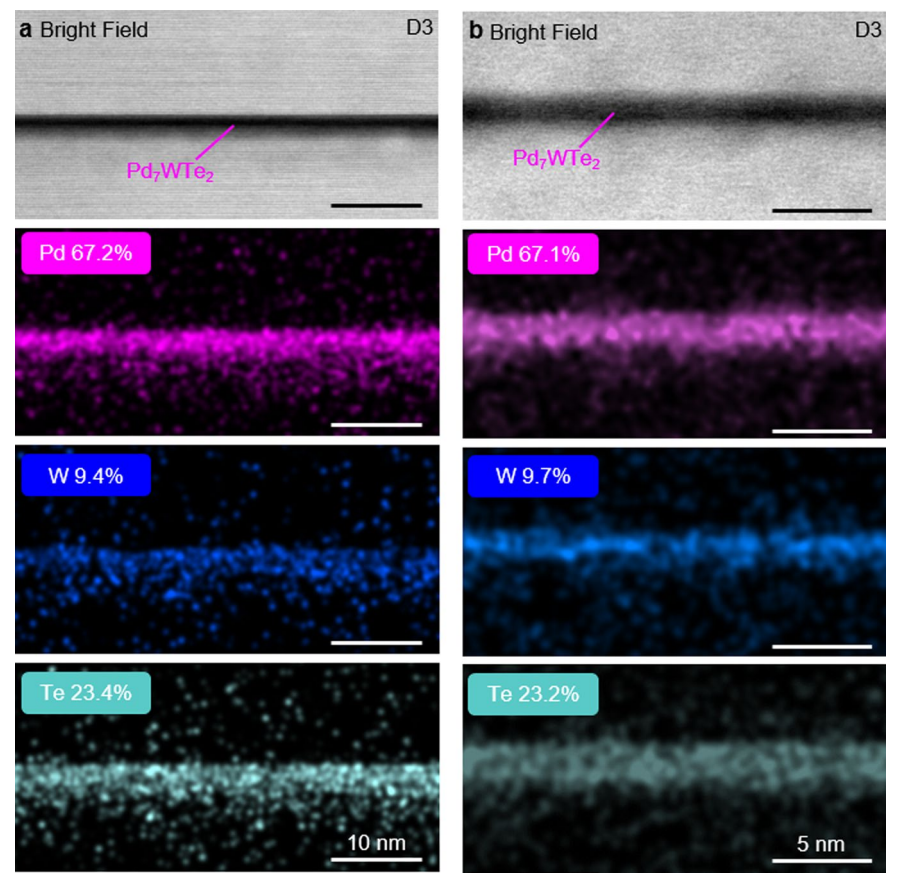
D4 Spot2	Atomic fraction (%)			
	Pd	W	Те	
Area 1	68.8	11.1	20.1	
Area 2	1.6	32.6	65.8	

Extended Data Fig. 3 | Additional EDX analyses and elemental mappings on D4. a,b, The HAADF STEM images and corresponding EDX elemental mappings on monolayer WTe₂ and Pd₇WTe₂ at two additional locations on D4. The extracted

b HAADF		Pd
1Ľ WTe ₂	Pd ₇ WTe ₂	W
Area 3	Ann #	Te
	25 nm	<u>50 nm</u>

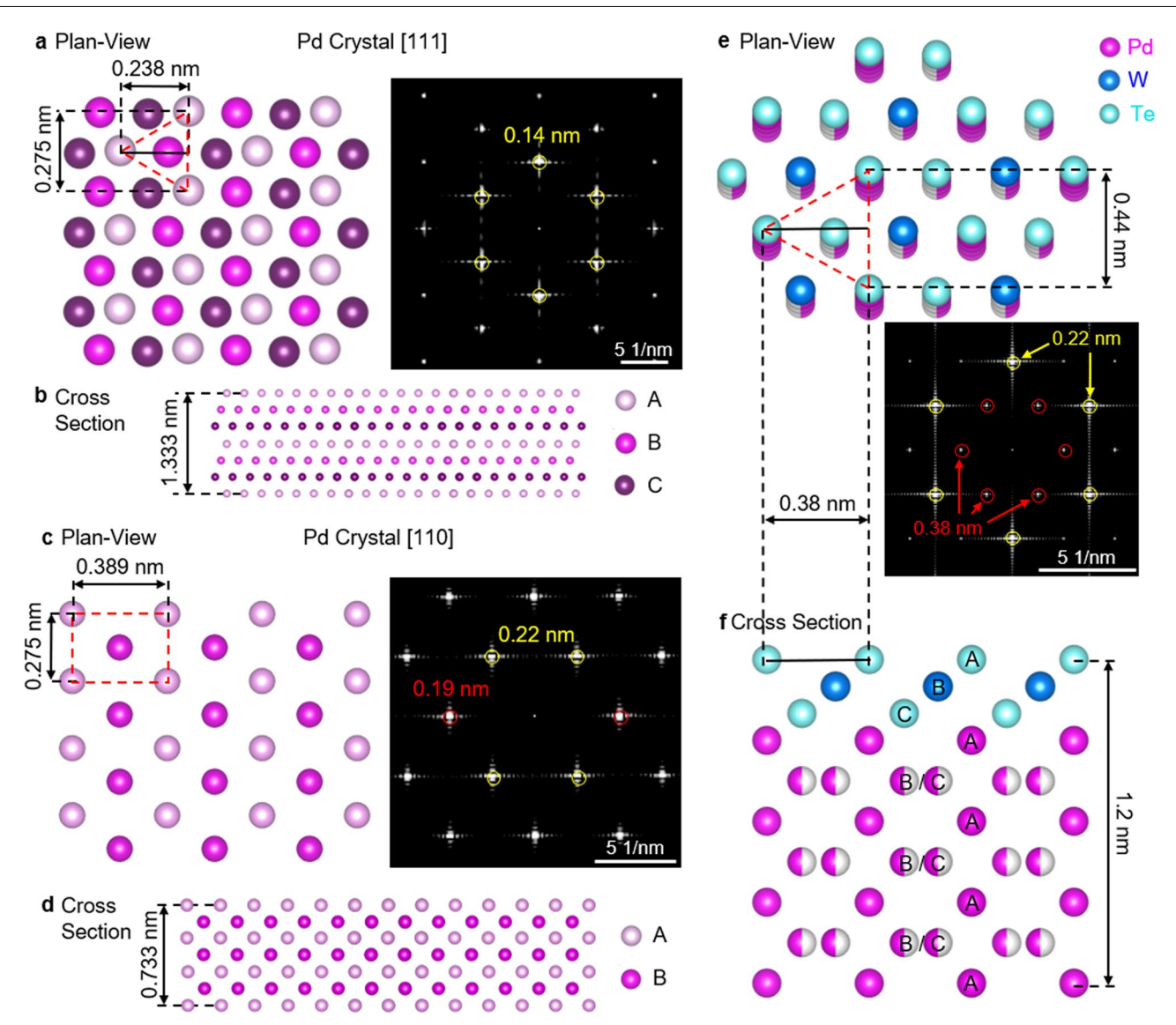
D4 Spot3	Atomic fraction (%)			
	Pd	W	Те	
Area 3	2.0	33.0	65.0	
Area 4	68.8	10.3	20.9	

atomic fractions of selected areas are summarized in the tables. The Pd:W:Te atomic ratios in Pd propagated regions are always found to be approximately 7:1:2



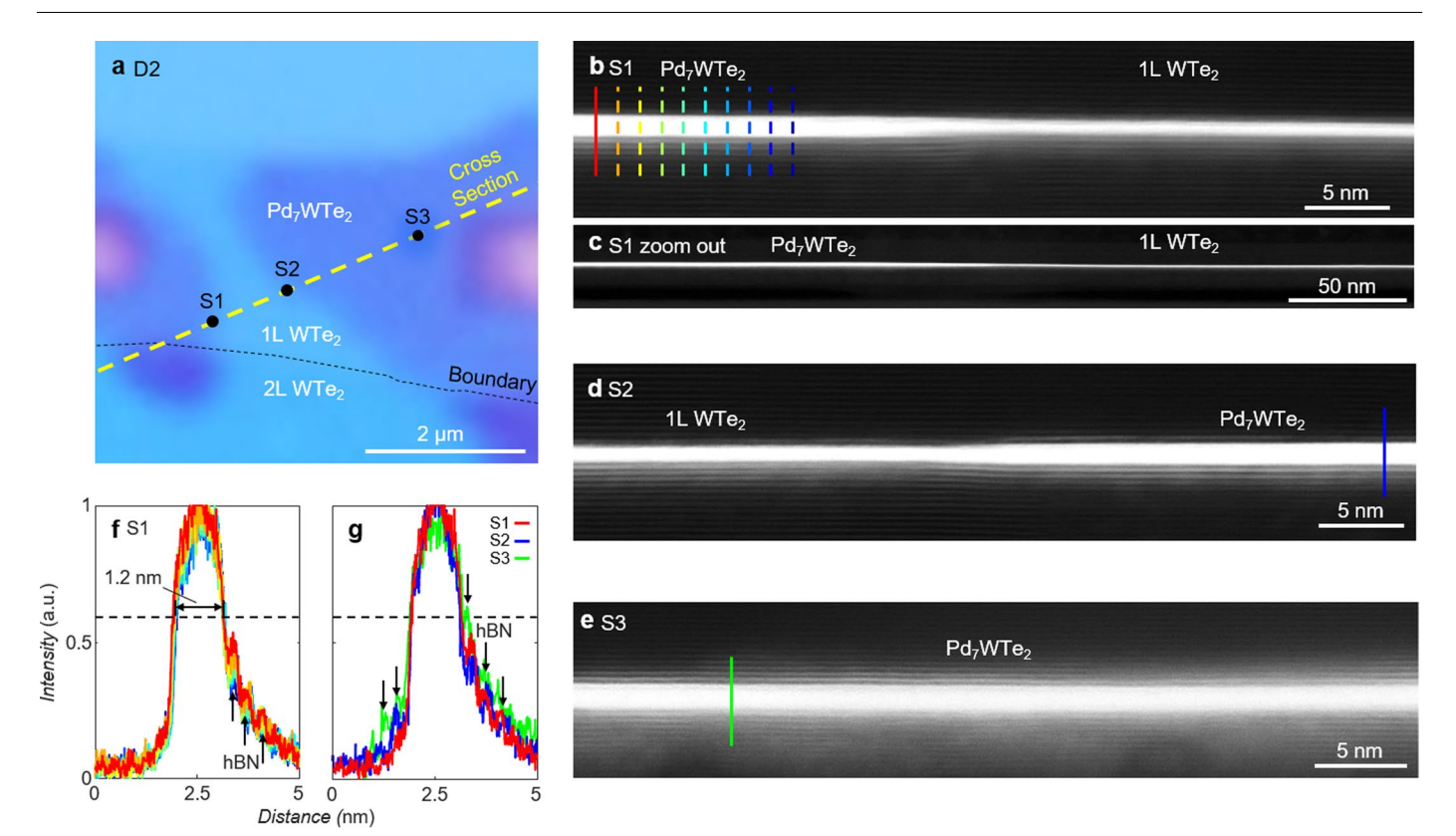
Extended Data Fig. 4 | Additional EDX analyses and elemental mappings on the cross-sections of D3. a,b, The bright field images and corresponding EDX elemental mappings on another 2 locations of D3 with Pd_7WTe_2 synthesized from

monolayer WTe $_2$. The Pd:W:Te atomic ratio is found to be close to 7:1:2. The small deviations may be the result of insufficient signal intensity in the cross-section measurements.



Extended Data Fig. 5 | Bulk Pd crystal versus the proposed crystal structure of Pd $_7$ WTe $_2$. a, An FCC bulk Pd crystal viewed along the [111] direction. Pd atoms from different layers are colored in different shades. The plan-view of such structure exhibits six-fold symmetry, as is shown by the simulated diffraction pattern (right panel). b, Cross-section of 7-layers of Pd atoms organized in the structure corresponding to a. c, The Pd crystal viewed along the [110] direction, which consists of alternatively stacked (A-B-A) rectangular lattices. Again, Pd atoms from different layers are shaded differently for a better visualization. The

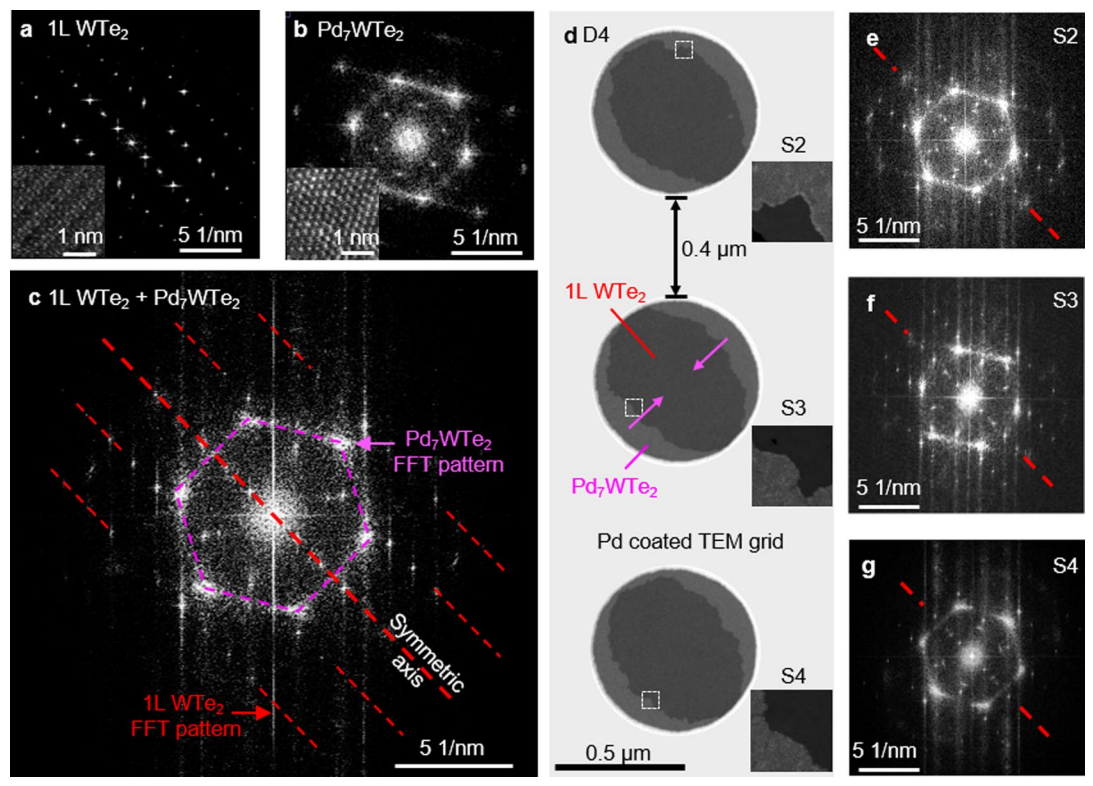
resulting plan-view lacks six-fold symmetry. The distorted hexagon is clearly seen in the simulated diffraction pattern (right panel). \mathbf{d} , Cross-section of 7-layers of Pd atoms organized in the structure corresponding to \mathbf{c} . \mathbf{e} , \mathbf{f} , The plan-view (top panel) and cross-section (bottom panel) of our proposed crystal structure for Pd₇WTe₂, consisting of 10 layers of hexagonal lattices, with the stacking order and atom species indicated. The half-colored atoms indicate that these sites are only filled 50 %. The simulated plan-view diffraction pattern (middle panel) captures characteristic features of experimental results.



Extended Data Fig. 6 | Uniform thickness of monolayer seeded Pd₇WTe₂.

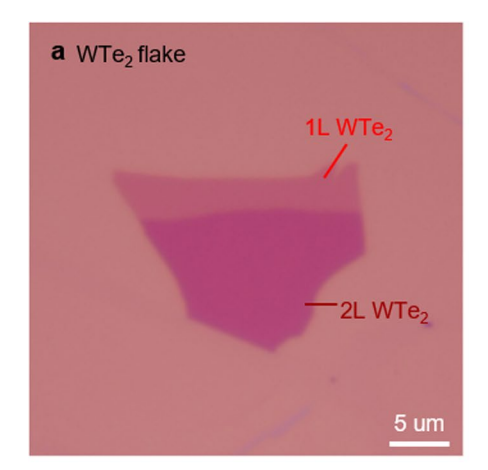
 ${\bf a}$, An optical image of the target region of device D2, focusing on the monolayer WTe $_2$ and Pd $_7$ WTe $_2$ areas. STEM measurements were performed along the cross-section cut indicated by the yellow dashed line. Spots S1, S2 and S3 are estimated locations under examination in ${\bf b}\text{-}{\bf e}$. ${\bf b}$, A HAADF STEM image captured at spot S1, which interfaces monolayer WTe $_2$ and Pd $_7$ WTe $_2$. The extracted intensity along the colored line-cuts is shown in ${\bf f}$. ${\bf c}$, The zoomed-out STEM image at spot S1, showing the uniform thickness on the scale of -100 nm. ${\bf d}$, A HAADF STEM image

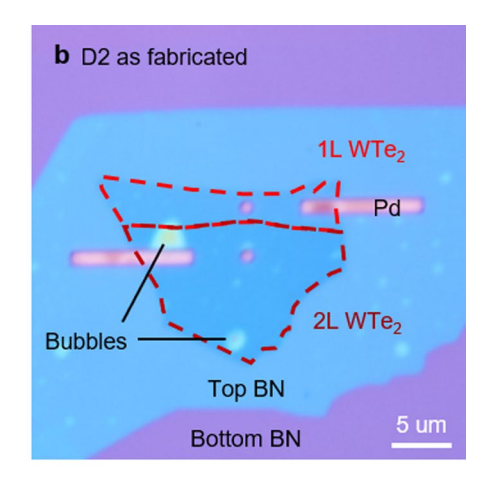
acquired at the interface between monolayer Pd_7WTe_2 and WTe_2 at spot S2. ${\bf e}$, A HAADF STEM image obtained at spot S3. ${\bf f}$, The extracted intensity from S1 along the line-cuts in ${\bf b}$, indicated by the vertical lines. The signal from hBN layer structure is indicated by arrows. ${\bf g}$, The extracted intensity from S1-S3 along line-cuts indicated by the solid lines in ${\bf b}$, ${\bf d}$ & ${\bf e}$. The data confirms that the thickness of Pd_7WTe_2 is uniform on the same monolayer seed, even the Pd comes from separate sources.

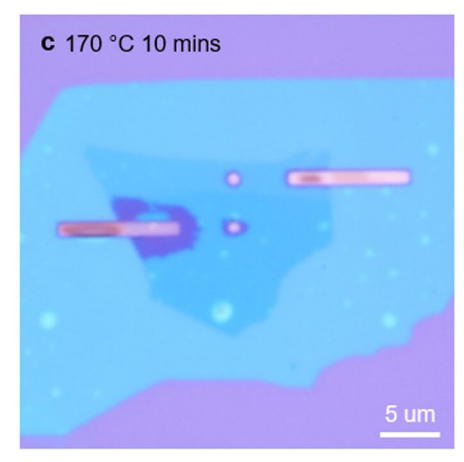


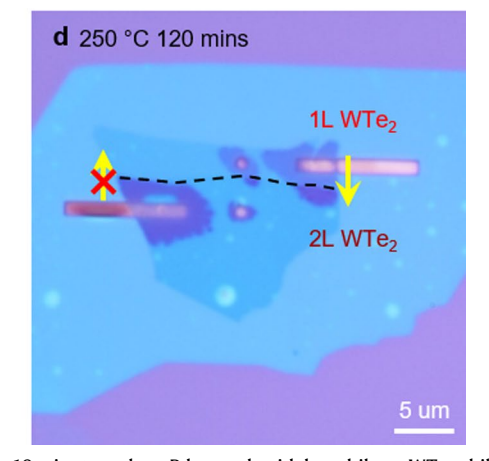
Extended Data Fig. 7 | The locked orientation of Pd₂WTe₂ lattices and monolayer WTe₂. a, The FFT pattern and atomic-resolution image (inset) of monolayer WTe₂ crystal. b, The FFT pattern and atomic-resolution image (inset) of monolayer seeded Pd₇WTe₂. c, An FFT pattern of the interfacing region (S1, Fig. 3b) including both monolayer WTe₂ and Pd₇WTe₂. The resulting FFT pattern exhibits characteristic features of both materials, highlighted separately by dashed lines (red for WTe₂, purple for Pd₇WTe₂). It is noted that their FFT

patterns are aligned with specific angles and symmetric about the indicated symmetric axis. \mathbf{d} , STEM images of another three additional spots, S2-S4, selected from three separated TEM grid holes. The locations of the three spots are indicated by white dashed boxes. $\mathbf{e}-\mathbf{g}$, The FFT patterns of S2-S4, which exhibit same orientation relation between monolayer WTe₂ and Pd₇WTe₂ lattice. The data shows that the Pd₇WTe₂ lattice orientation is determined by the seed monolayer WTe₂.



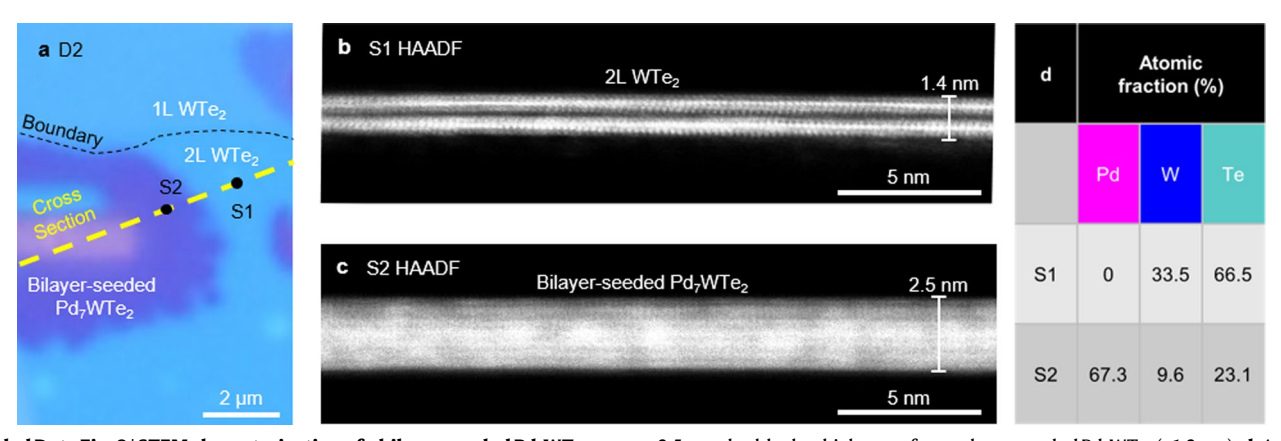






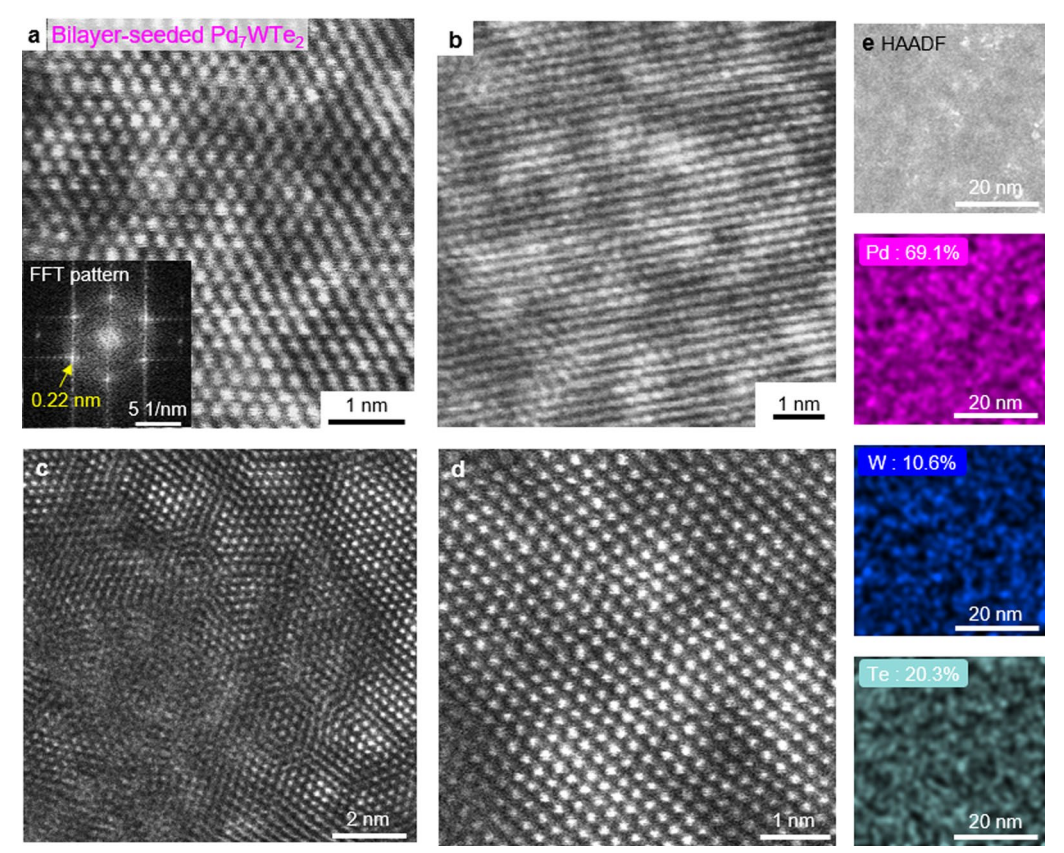
Extended Data Fig. 8 | **Pd transport on monolayer and bilayer WTe**₂. **a**, Optical image of a WTe₂ flake with both monolayer and bilayer regions. **b**, Optical image of device D2 as fabricated, where monolayer and bilayer WTe₂ are in contact with separate Pd sources. **c**, Optical image of D2 after being held at 170 °C for

10 minutes, where Pd spreads widely on bilayer WTe $_2$ while not noticeable on monolayer WTe $_2$. \mathbf{d} , Optical image of D2 after being held at 250 °C for 120 minutes, showing Pd transport from monolayer WTe $_2$ to bilayer WTe $_2$, but not vice versa.



Extended Data Fig. 9 | **STEM characterization of a bilayer-seeded Pd**₇**WTe**₂. **a**, A zoom-in optical image of device D2, focusing on the bilayer WTe₂ and bilayer-seeded Pd
₇**WTe**₂ areas. STEM measurements were performed along the cross-section line (yellow line) and images were obtained at estimated spots S1 and S2, as indicated. **b**, HAADF STEM cross-section image of bilayer WTe
₂ at location S1, where the vdW gap is clearly observed. **c**, HAADF STEM cross-section image of bilayer-seeded Pd
₇**WTe**₂ at location S2. The thickness is measured to be

 $2.5\,\text{nm}$, double the thickness of monolayer-seeded Pd_7WTe_2 ($-1.2\,\text{nm}$). \boldsymbol{d} , Atomic fractions for bilayer WTe_2 and bilayer-seeded Pd_7WTe_2 from EDX analysis. We did not obtain atomic resolution in the STEM images of the bilayer-seeded Pd_7WTe_2 region, which we suspect might be a result of in-plane domain inhomogeneity. Future improvements are necessary for obtaining an image with atomic resolution.



Extended Data Fig. 10 | In-plane lattice structure and atomic fraction of bilayer-seeded Pd, WTe₂. a, An atomic-resolution STEM plan-view image of bilayer-seeded Pd, WTe₂, which displays similar hexagonal lattice as monolayer seeded Pd, WTe₂. The FFT pattern of such lattice is shown in the inset. \mathbf{b} - \mathbf{d} ,

Selected lattice structures observed in other locations of bilayer-seeded $Pd_{7}WTe_{2}$, indicating the presence of non-uniform domain structures. \mathbf{e} , Elemental mappings and atomic fraction of bilayer-seeded $Pd_{7}WTe_{2}$.